Quantification of the ferric/ferrous iron ratio in silicates by scanning transmission X-ray microscopy at the Fe L2,3 edges

Franck Bourdelle, Karim Benzerara, Olivier Beyssac, Julie Cosmidis, Daniel R. Neuville, Gordon E. Brown Jr., Erwan Paineau

1 Quantification of the ferric/ferrous iron ratio in silicates by scanning transmission x-ray

2 microscopy at the Fe $L_{2,3}$ edges

3

4 Authors: Franck Bourdelle [a,b], Karim Benzerara [a], Olivier Beyssac [a], Julie Cosmidis [a], Daniel

5 Neuville [c], Gordon E. Brown Jr [d,e], Erwan Paineau [f,g]

6

7 Mailing addresses of the relevant institutions:

8

9 [a] IMPMC, UPMC-CNRS, Case courrier 115, 4 Place Jussieu, 75252 Paris cedex 05, France

10 [b] GeoRessources, Université de Lorraine, UMR 7359 CNRS, 54506 Vandœuvre-lés-Nancy,

11 France

12 [c] Géochimie et Cosmochimie, Institut de Physique du Globe de Paris, Université Paris

13 Diderot, Sorbonne Paris Cité, UMR 7154 CNRS, 1 rue Jussieu 75005 Paris, France

14 [d] Surface & Aqueous Geochemistry Group, Department of Geological and Environmental

15 Sciences, Stanford University, Stanford, CA, 94305-2115, USA

16 [e] SLAC Natl Accelerator Lab, Stanford Synchrotron Radiation Lightsource, Menlo Pk, CA

17 94025 USA

18 [f] Laboratoire de Physique des Solides, Université Paris-Sud, UMR 8502 CNRS, Bâtiment

19 510, 91405 Orsay cedex, France

20 [g] CEA Saclay, IRAMIS, Laboratoire Interdisciplinaire sur l'Organisation Nanométrique et

21 Supramoléculaire, 91191 Gif-sur-Yvette cedex, France

22

23 Corresponding authors:

24 1. Franck Bourdelle

25 Present mailing address: GeoRessources, Université de Lorraine, UMR 7359 CNRS, 54506

26 Vandœuvre-lés-Nancy, France

27 E-mail address: franck.bourdelle@gmail.com

28 Phone number: + 33 (0)3 83 68 47 28

29

30 2. Karim Benzerara

31 Mailing address: IMPMC, UPMC-CNRS, Case courrier 115, 4 Place Jussieu, 75252 Paris

32 cedex 05, France

33 E-mail address: Karim.Benzerara@impmc.upmc.fr

34 Phone number: + 33 (0)1 44 27 75 42

35

36 **Abstract**

37

38 Estimation of $Fe^{3+}/\Sigma Fe$ ratios in materials at the submicrometer scale has been a long-standing

39 challenge in the Earth and environmental sciences because of the usefulness of this ratio in

40 estimating redox conditions as well as for geothermometry. To date, few quantitative methods

41 with submicrometric resolution have been developed for this purpose, and most of them have

42 used electron energy-loss spectroscopy (EELS) carried out in the UHV environment of a

43 transmission electron microscope (TEM). Scanning transmission x-ray microscopy (STXM)

44 is a relatively new technique complementary to TEM and is increasingly being used in the

45 Earth sciences. Here, we detail an analytical procedure to quantify the $Fe^{3+}/\Sigma Fe$ ratio in

46 silicates using Fe $L_{2,3}$-edge x-ray absorption near edge structure (XANES) spectra obtained by

47 STXM, and we discuss its advantages and limitations. Two different methods for retrieving

48 $Fe^{3+}/\Sigma Fe$ ratios from XANES spectra are calibrated using reference samples with known Fe^{3+}

49 content by independent approaches. The first method uses the intensity ratio of the two major

50 peaks at the L_3-edge. This method allows mapping of $Fe^{3+}/\Sigma Fe$ ratios at a spatial scale better

51 than 50 nm by the acquisition of 5 images only. The second method employs a 2-eV-wide

52 integration window centred on the L_2 maximum for Fe^{3+}, which is compared to the total

53 integral intensity of the Fe L_2-edge. These two approaches are applied to metapelites from the

54 Glarus massif (Switzerland), containing micrometer-sized chlorite and illite grains and

55 prepared as ultrathin foils by Focused Ion Beam milling. Nanometrer-scale mapping of iron

56 redox in these samples is presented, and shows evidence of compositional zonation. The

57 existence of such zonation has crucial implications for geothermometry and illustrates the

58 importance of being able to measure $Fe^{3+}/\Sigma Fe$ ratios at the submicrometer scale in geological

59 samples.

60

61 Keywords: ferric/ferrous iron, STXM, XANES spectroscopy, $L_{2,3}$-edge, redox mapping,

62 silicate.

63

64 **Introduction**

65

66   Determination of the redox state of iron and its spatial variations in sediments and

67 rocks is of critical importance in both geosciences and environmental sciences, because of the

68 need to understand redox state during their deposition or formation as well as subsequent

69 changes in redox state due to weathering and other processes (e.g., de Andrade et al. 2006;

70 Muñoz et al. 2006; Bernard et al. 2010; Benzerara et al. 2011; Bolfan-Casanova et al. 2012;

71 Stagno et al. 2013). In addition, quantification of $Fe^{3+}/\Sigma Fe$ ratios can yield a better insight into

72 the chemistry of complex geological materials (e.g., Muñoz et al. 2006), or a better estimation

73 of *P-T* conditions by geothermobarometers, when variations of the Fe^{3+} content within the

74 crystals are taken into account (e.g., Schmid et al. 2003; de Andrade et al. 2006; Bourdelle et

75 al. 2013a). Therefore, assessment of the $Fe^{3+}/\Sigma Fe$ ratio in minerals is an important and long-

76 standing issue. Different techniques have been used extensively in the past for this purpose,

77 including electron microprobe analysis (EMPA, e.g., Fialin et al. 2004), Mössbauer

78 spectroscopy (e.g., Beaufort et al. 1992) x-ray photoelectron spectroscopy (XPS, e.g.,

79 Raeburn et al. 1997a, b), or x-ray absorption near edge structure (XANES) spectroscopy at

80 the K edge (e.g., Waychunas et al. 1983; Bajt et al. 1994; Wilke et al. 2001, 2009; Berry et al.

81 2003, 2010). However, none of these methods provides spatial resolution at the few

82 nanometers scale, which is particularly useful for studying chemical zonations patterns

83 observed in low-temperature systems. Several studies (e.g., van Aken and Liebscher, 2002)

84 have shown that electron energy-loss spectroscopy (EELS) carried out in a transmission

85 electron microscope (TEM) is a powerful method for determining the redox state of iron at a

86 submicrometer resolution. However it sometimes induces severe beam damage effects, such

87 as electron beam-induced oxidation of iron (Lauterbach et al. 2000; Garvie et al. 2004), the

88 effect of which can be corrected by measuring the signal as a function of time. Alternatively,

89 XANES spectroscopy at the Fe $L_{2,3}$ edges carried out with a scanning transmission x-ray

90 microscope (STXM) has been increasingly used in the Earth and environmental sciences to

91 infer qualitatively $Fe^{3+}/\Sigma Fe$ ratios in geological and environmental samples at a spatial

92 resolution of ~50-nm (e.g., Wasinger et al. 2003; Carlut et al. 2010; Lam et al. 2010; de Groot

93 et al. 2010; Miot et al. 2011; Boulard et al. 2012). This technique has several advantages such

94 as offering a high energy resolution (better than 0.1 eV at existing synchrotron facilities) and

95 the possibility of maintaining samples under anoxic conditions before and during the

96 measurement (e.g., Miot et al. 2009). However, no calibration of the STXM-based Fe $L_{2,3}$-

97 edge XANES approach has yet been carried out, whereas calibration of the EELS approach

98 was quantified by van Aken and Liebscher (2002). Fe $L_{2,3}$-edges result from $2p \rightarrow 3d$

99 electronic transitions, as shown by Wasinger et al. (2003). These authors described in detail

100 the physical basis of Fe L edges, and showed that information about iron valency can be

101 retrieved from XANES spectra by a multiplet calculation approach (e.g., van der Laan and

102 Kirkman, 1992; Cressey et al. 1993). This approach is difficult to apply when dealing with

3

103   mineral phases for which we do not know the structure. Alternatively, fitting of XANES

104   spectra with a linear combination of normalized reference spectra has been performed by Miot

105   et al. (2009), but requires appropriate Fe^{2+} and Fe^{3+} end-member reference compounds with

106   Fe in the same local coordination environment as in the sample of interest. Van Aken and

107   Liebscher (2002) have shown the possibility of a third approach that they calibrated for EELS

108   and which uses an empirical correlation between $Fe^{3+}/\Sigma Fe$ ratios and a parameter (i.e.,

109   modified integral white-line intensity ratio) which is directly retrieved from EELS spectra at

110   the Fe $L_{2,3}$ edges, and is independent of the coordination environment of Fe to a the first-order

111   approximation.

112   Here we propose an empirical approach similar to that of van Aken and Liebscher

113   (2002) to calibrate the correlation between $Fe^{3+}/\Sigma Fe$ ratio and some parameters extracted from

114   the STXM-derived XANES Fe $L_{2,3}$-edge spectra of reference silicate glasses and

115   phyllosilicates. Two empirical calibrations are proposed, both of which offer a compromise

116   between speed and accuracy of the analytical measurement. An application of this approach to

117   ultra-thin sections of natural chlorites and micas is presented to illustrate the methodology and

118   to further assess the range of applicability of this calibration for STXM.

119

120   **Materials and Methods**

121

122   *Reference samples*

123

124   The samples used in this study were reference synthetic silicate glasses, natural

125   phyllosilicates and fayalite, prepared as powders or ultra-thin sections cut by Focused Ion

126   Beam (FIB) milling. The bulk chemical compositions of the five synthetic glasses were

127   previously determined by Magnien et al. (2004). All samples are composed of similar

128   proportions of Si, Mg, Ca, Na and Fe. The SiO_2 and FeO contents are ~52 wt% and ~13 wt%,

129   respectively. Bulk $Fe^{3+}/\Sigma Fe$ ratios were determined by wet chemistry, Mössbauer

130   spectroscopy and EMPA and range from 0.09 to 0.94 (Table 1; Magnien et al. 2004). For

131   STXM-XANES analyses, we ground these samples in deaerated and deionized water, inside

132   an anoxic glovebox ($p(O_2) < 50$ ppm) to avoid oxidation during sample preparation.

133   The phyllosilicate samples have 2:1 and 2:1:1 structures and their bulk compositions

134   were investigated previously by Joswig et al. (1986), Keeling et al. (2000), Shingaro et al.

135   (2005), Rigault et al. (2010), and in the present study by EMP analyses. Total Fe contents

136   vary significantly between samples and bulk $Fe^{3+}/\Sigma Fe$ ratios ranging between 0.03 and 1.0

4

137   were measured by Mössbauer spectroscopy, EXAFS (extended x-ray absorption fine

138   structure) and/or EELS (Table 1). In addition, a fayalite sample was used as a pure Fe^{2+}

139   reference. For STXM-XANES analyses, some samples (smectite Nau-2, chlorites GAB 42,

140   VNI 92, VNI 114, fayalite) were prepared by grinding in deaerated and deionized water in an

141   anoxic glovebox ($p(O_2) < 50$ ppm). Other samples (clintonite, chlorite 'prochlorite', chlorite

142   Ch1, Ti-mica) where prepared by FIB milling.

143   Samples transparent to soft x-rays are needed to measure XANES spectra in the

144   transmission mode of STXM, therefore requiring the preparation of thin samples. FIB foils

145   were cut with a FEI Model 200 TEM FIB system at University Aix-Marseille using the

146   protocol detailed by Heaney et al. (2001). A 30 kV Ga^+ beam operating at ~20 nA excavated

147   the sample to a depth of 5 μm. The sample foil was then further thinned to ~80-100 nm at

148   lower beam voltage (5 kV) and current (~100 pA), in order to remove the layer damaged by

149   high-energy ions (Bourdelle et al. 2012).

150

151   *Glarus field samples*

152

153   The Glarus Alps (Switzerland) belongs to the Helvetic zone of the northern margin of

154   the Central Alps, and was affected by low-grade metamorphism. Details about the location

155   and composition of the samples analyzed by STXM in the present study are provided in

156   Lahfid et al. (2010). The selected rock samples are metapelites, more or less clayey or sandy

157   marls, with various proportions of quartz, calcite, and clay minerals. Three samples (noted

158   Glarus GL07 13, 16, and 20, as in Lahfid et al. 2010), containing chlorites and K-deficient

159   micas, were milled by FIB. The compositions of the chlorites and micas were obtained on the

160   FIB foils by analytical electron microscopy analyses described elsewhere (Bourdelle et al.

161   2012).

162

163   *XANES spectroscopy*

164

165   Part of the STXM analyses were performed at the Advanced Light Source (ALS)

166   (Lawrence Berkeley National Laboratory) on branch line 11.0.2.2 following the procedures

167   described in Miot et al. (2009). The ALS storage ring was operated at 1.9 GeV and 500 mA

168   current in a top-up mode. More details on the branch line 11.0.2.2 and beam characteristics

169   are given by Bluhm et al. (2009). Stacks of images were obtained by scanning the sample in

170   the x–y directions of selected sample areas over the 690–730 eV energy range (Fe $L_{2,3}$-edge)

171   using an energy increment of 0.789 eV between 690 and 705 eV, 0.10 eV in the 705–713 eV

172   energy range, 0.19 eV in the 713–719 eV energy range, 0.155 eV in the 719-726 eV energy

173   range, and 0.475 eV in the 726-730 eV energy range. The dwell time per pixel and energy

174   point was 1.3 ms.

175   Some data (chlorite Ch1, chlorite 'prochlorite' and Ti-mica) were acquired on the

176   Pollux beamline at the Swiss Light Source (SLS, Villigen, Switzerland). The SLS synchrotron

177   storage ring was operated at 2.4 GeV and 300 mA current in a top-up mode during data

178   collection, and the characteristics of the beamline are detailed by Raabe et al. (2008). Stacks

179   were obtained over the 690–730 eV energy range (Fe $L_{2,3}$-edge) using an energy increment of

180   0.667 eV between 690 and 700 eV, 0.15 eV in the 700–715 eV energy range, 0.40 eV in the

181   715–727 eV energy ranges, and 0.89 eV in the 727-730 eV energy range. The dwell time per

182   pixel and energy point was 3.5 ms.

183   At both the ALS and the SLS, focus was achieved systematically for each sample, and

184   precision in the determination of the focus position was better than the focus depth. Image

185   stacks were aligned and XANES spectra were derived from areas of interest using the

186   aXis2000 software (Hitchcock, 2012). Potential beam damage caused by the incident photon

187   beam was assessed by monitoring spectral changes at the Fe $L_{2,3}$-edge with increasing dwell

188   times up to a hundred milliseconds (10, 50, and 100 ms).

189

190   *Spectra processing*

191

192   Energy calibration was performed using the gaseous neon $1s \rightarrow 3p$ electronic

193   transition at 867.3 eV. As explained in Figure 1, the processing of spectra consisted of two

194   steps. First, the contribution of lower energy absorption edges (i.e., background) was removed

195   so that in the end, the pre-edge region is set to 0 optical density (noted OD) with a slope of

196   zero. For that purpose, a "linear background" correction was applied to the spectrum. Second,

197   the two edge steps resulting from transitions to unoccupied states in the continuum were

198   subtracted using the following double arctan function (Chen et al. 1995; van Aken and

199   Liebscher, 2002; Brotton et al. 2007):

200

201    $$f(\Delta E) = \frac{h_1}{\pi}\left(\arctan\left[\frac{\pi}{w_1}(\Delta E - E_1) \right] + \frac{\pi}{2} \right) + \frac{h_2}{\pi}\left(\arctan\left[\frac{\pi}{w_2}(\Delta E - E_2) \right] + \frac{\pi}{2} \right) \qquad (1)$$

202

203 where h_1 and h_2 are the step heights of the two arctan functions, w_1 and w_2 are fixed peak

204 widths, and E_1 and E_2 are the positions of the inflection points resulting in an energy near the

205 edge onset. Here, w_1 and w_2 are fixed to 1 eV (Fig. 1). Brotton et al. (2007) proposed setting

206 the function slope w at 5 eV, to account for the slow onset of the continuum. They argued that

207 a value smaller than 5 eV could induce spurious structures in the background-corrected

208 spectrum. We observed that values of $w = 1$ eV or $w = 5$ eV provided similar results.

209

210 **Results and Discussion**

211

212 *Evolution of Fe $L_{2,3}$–edge XANES spectra with changes in* $Fe^{3+}/\Sigma Fe$

213

214   XANES spectra at the Fe $L_{2,3}$-edges of the reference phyllosilicates, fayalite and five

215 Fe-bearing silicate glasses, corrected for continuum absorption, are shown in Figure 2, and the

216 positions of major peaks are summarized in Table 1. These spectra are qualitatively similar to

217 those described in several previous studies and were obtained using different analytical

218 techniques (e.g., Crocombette et al. 1995; Heijboer et al. 2003; van Aken and Liebscher,

219 2002). Four major Fe $L_{2,3}$-edge XANES peaks are present in all samples. The two major

220 peaks on the L_3 edge are noted as "L_3-a" and "L_3-b", and similarly, the major peaks on the L_2

221 edge are noted as "L_2-a" and "L_2-b". For all samples examined, the measured separations of

222 the Fe L_3 and L_2 maxima, due to spin-orbit splitting (van Aken and Liebscher, 2002), are 12.9

223 $\pm$ 0.4 eV and 14.2 $\pm$ 1.4 eV for peaks a and b, respectively in agreement with previous EELS

224 and XANES studies (e.g., de Smit et al. 2008; de Groot et al. 2010). However, although most

225 of the spectra show a single asymmetrical L_3-a peak, some of them (i.e., VNI 92, VNI 114

226 and GAB 42, fayalite) display an "L_3-a" split into two peaks. In addition, these specific

227 spectra show additional peaks on the L_3-a side at ~706.3 and ~706.8 eV. According to

228 Wasinger et al. (2003), the presence of these minor peaks may be due to a specific atomic

229 environment and/or orbital co-valency of iron in these mineral phases. Similarly, several

230 minor peaks can be observed at around 719.8 eV on the L_2-edge for several samples (VNI 92,

231 VNI 114, GAB 42, PyrNa 17R, fayalite).

232   The relative intensities of the different major peaks vary depending on the $Fe^{3+}/\Sigma Fe$

233 ratio (Figure 2). With increasing $Fe^{3+}/\Sigma Fe$ ratios, the relative intensity of the L_3-a peak

234 decreases compared to that of the L_3-b peak; L_3-a is more intense than L_3-b in the XANES

235 spectrum of the VNI 92 sample ($Fe^{3+}/\Sigma Fe = 0.35$), whereas the opposite is observed for PyrNa

7

236   5R ($Fe^{3+}/\Sigma Fe = 0.61$). Likewise, the relative intensity of L_2-a progressively decreases whereas

237   that of L_2-b increases as $Fe^{3+}/\Sigma Fe$ increases. The energy position of L_2-b changes very little

238   between the samples, whereas peaks L_3-a and L_2-a shift slightly towards higher energies when

239     $Fe^{3+}/\Sigma Fe$ increases.

240

241   *Quantification of $Fe^{3+}/\Sigma Fe$ from XANES Fe $L_{2,3}$-edge intensity ratios*

242

243   As documented in Figure 2, the main variations in the XANES spectra of reference

244   samples with varying $Fe^{3+}/\Sigma Fe$ ratios involve the L_3-b/L_3-a intensity ratio. More precisely, the

245   L_3-b/L_3-a intensity ratio is linearly correlated with $Fe^{3+}/\Sigma Fe$ ratio with only a little scatter (R^2

246     $= 0.96$) for both the phyllosilicates and silicate glasses (Figure 3). The correlation is described

247   by equation (2):

248

249     $$\frac{Fe^{3+}}{\sum Fe} = \frac{R_{L_3} - 0.1867}{0.01991} \qquad \text{with} \qquad R_{L_3} = \frac{I(L_3 - b)}{I(L_3 - a)} \qquad (2)$$

250

251   This approach requires only five XANES images to map $Fe^{3+}/\Sigma Fe$ (see Figure 4 and below):

252   two images in the pre-edge (needed to apply the "linear background correction" at each pixel

253   of the image), one at 708.7 eV to quantify the L_3-a peak, one at 710.25 eV to quantify the L_3-

254   b peak, and one at 718 eV, to remove the edge step of the arctan function. Finally, the ratio of

255   the resulting 708.7 and 710.25 eV images can be used to determine the R_{L3} parameter at each

256   pixel of the image.

257   This calibration is useful but has some limitations. The L_3 peaks, which are much

258   more intense than the L_2 peaks, are more susceptible to absorption saturation (see Hanhan et

259   al. 2009, where saturation effects are described for Ca 2p edge spectra). This phenomenon

260   occurs when the sample is too thick and/or highly concentrated in Fe implying that few

261   photons are transmitted. This may trigger a non-linear response of the detection and an

262   artifactual modification of the relative peak heights. The use of a spectral parameter correlated

263   with $Fe^{3+}/\Sigma Fe$ based on the less absorbing L_2-edge may provide in this case an interesting way

264   of circumventing absorption saturation issues encountered with the L_3-edge.

265   Figure 2 shows that an increase of $Fe^{3+}/\Sigma Fe$ is associated with a decrease of the

266   intensity of L_2-a. Figure 5 shows the correlation between $Fe^{3+}/\Sigma Fe$ and R_{L2}, a ratio that reflects

267   the importance of L_2-b relative to the total L_2. Similar to the modified intensity defined by van

268   Aken and Liebscher (2002), the L_2-b contribution is computed as an integration window of 2

269   eV width centred around the maximum L_2-b intensity; the ratio R_{L2} is calculated from this

270   modified L_2-b intensity and the total integral intensity of L_2-edge. The correlation is high (R^2

271   $= 0.97$), and is described by equation (3):

272

273   $$\frac{Fe^{3+}}{\sum Fe} = \frac{R_{L_2} - 0.1476}{0.00297} \qquad \text{with} \qquad R_{L_2} = \frac{I(L_2 - b)_{mod}}{A(L_2)_{total}} \qquad (3)$$

274

275   This approach requires the acquisition of a complete stack of images (i.e., as many images as

276   energy points are required to obtain a complete spectrum with a given spectral resolution)

277   between 715 and 730 eV, to cover the entire L_2-edge, and to calculate the double arctan

278   function (equation (1)). As a consequence, the acquisition time required for this method is

279   longer than for the L_3-b/L_3-a intensity ratio method (e.g. 30-40 min *versus* 5-10 min for an

280   area of 150 by 150 pixels). However, this second method seems to be more accurate,

281   especially because (1) the calibration data are less scattered (Fig. 5 *versus* Fig. 3) and (2) the

282   intensity integration improves the signal-to-noise ratio. Several other methods of calibration

283   have been tested, sometimes giving equation with a high correlation (with a R^2 up to 0.95),

284   but the two methods proposed here seem to be a good trade-off between $Fe^{3+}/\Sigma Fe$ estimation

285   accuracy, acquisition time and ease of use.

286

287   *Assessment of saturation and beam damage effects*

288

289   When particles are sufficiently thin, the intensity of each spectral feature changes

290   linearly with thickness. However, Hanhan et al. (2009) showed that in the case of samples that

291   are too thick, one can observe distortions of the Ca 2p spectrum due to a saturation effects.

292   These observations led the authors of that study to set a maximum peak intensity, which

293   should not be exceeded to avoid saturation phenomena.

294   Similarly, we determined the maximum peak intensity below which the Fe L_{23} spectra

295   are undistorted and vary linearly. For this purpose, a powder of the smectite Nau-2 sample

296   with grains of various sizes was analyzed by STXM. Figure 6 plots the difference between the

297   intensities at 710.35 (L_3-b) and 723.54 eV (L_2-b) (corrected from the pre-edge intensity) vs.

298   the intensity at 710.35 eV (L_3-b, i.e., the peak of maximum intensity for Nau-2, hence the

299   most susceptible to saturation) for each pixel of the stack of images (i.e., a total of 6336

300   pixels). The difference between L_3-b and L_2-b intensities increases linearly when L_3-b

301   intensity is lower than ~1.5 OD. Once the L_3-b intensity exceeds 1.5 OD, the L_3-b – L_2-b

9

302 difference increases more slowly than L_3-b, underlining (i) the distortion of the spectra for the

303 considered pixels, and (ii) the faster increase of L_2-b intensity compared to that of L_3-b with

304 increasing sample thickness. All the data presented in this study were therefore collected from

305 areas presenting a L_3 peak intensity lower than 1.5 OD.

306   The spectrum may be also influenced by the crystal orientation relative to the direction

307 of polarization of the x-ray beam, a process called linear dichroism. Therefore several

308 XANES spectra were measured on the same part of a FIB foil after sequential rotation of the

309 linear polarisation (see Benzerara et al., 2011 for details on the procedure). The variation of

310 resulting $Fe^{3+}/\Sigma Fe$ estimates is negligible, showing that sample orientation does not affect the

311 Fe^{3+} quantification.

312   Beam damage can also potentially alter assessment of the $Fe^{3+}/\Sigma Fe$ ratio. Here, beam

313 damage was evaluated by monitoring spectral changes at the Fe $L_{2,3}$-edge with increasing

314 dwell times from 10 up to 100 milliseconds. Figure 7 shows that $Fe^{3+}/\Sigma Fe$ ratios derived from

315 XANES spectra are only slightly affected by increasing dwell time. In particular, no

316 significant change was observed for typical dwell times used during routine analyses of the

317 samples (i.e., ~1.3 and 3.5 ms per energy- and image-point for ALS and SLS synchrotrons,

318 respectively).

319

320 *Application to a geological case: chlorites and micas from Glarus (Central Alps, Switzerland)*

321

322   To go further, we have applied the methods proposed here on micrometer-sized

323 chlorite and mica/illite-like grains sampled in the Glarus area of Switzerland and cut by FIB-

324 milling. The temperatures of chlorite formation were calculated from analytical electron

325 microscopy (AEM) chemical analyses, based on the thermometer by Bourdelle et al. (2013b),

326 which does not require $Fe^{3+}/\Sigma Fe$ input, and the thermometer by Inoue et al. (2009), which

327 needs a previous estimation of Fe^{3+} content. The $Fe^{3+}/\Sigma Fe$ ratios were estimated for each FIB

328 foil by XANES from equations (2) and (3). The results are given in Figure 8 and Table 2.

329   From images converted to optical density units taken at 708.7 eV, we can easily

330 distinguish Fe-rich and Fe-poor minerals: chlorites appear as light grey and represent the Fe-

331 rich phase, whereas micas are dark, i.e., Fe-poor. XANES spectra, acquired along the mica-

332 chlorite contacts show that the $Fe^{3+}/\Sigma Fe$ ratio is higher in illite than in chlorite: the $Fe^{3+}/\Sigma Fe$

333 ratios estimated by equation (3) range from 22.3% to 27.9% in chlorite, whereas these ratios

334 vary between 30 and 65.5% in illite-like phase. Equation (2) provides consistent estimations,

335 suggesting that both calibrations are reliable. This analysis shows that K-deficient micas can

10

336   contain a high proportion of ferric iron (e.g. samples 13 and 20). Despite the relatively high

337    $Fe^{3+}/\Sigma Fe$ ratio in some illite-like crystals, the total Fe^{3+} content remains higher in chlorite.

338   Figure 8 also shows the variations of $Fe^{3+}/\Sigma Fe$ ratios vs. the temperature of formation,

339   which was estimated by chlorite thermometry (Table 2). In this respect, $Fe^{3+}/\Sigma Fe$ ratio

340   increases slightly in chlorites with increasing temperature, whereas this ratio decreases in K-

341   deficient micas. It should be noted that, contrarily to the Bourdelle et al. (2013b) model, some

342   geothermometers based on thermodynamic models for chlorite (e.g., Inoue et al. 2009),

343   require prior determination of the $Fe^{3+}/\Sigma Fe$ ratio. When this value in not known, it is set to

344   zero as the default in these types of models. Interestingly, the comparison of results provided

345   by different thermometers in Table 2 shows that the Inoue and Bourdelle geothermometers

346   yield very different temperature results (differences of up to 76°C) when $Fe^{3+}/\Sigma Fe$ ratio is not

347   known. In contrast, taking into account the $Fe^{3+}/\Sigma Fe$, the two thermometers provide more

348   similar temperatures estimates (a maximum difference of less than 28°C, i.e., within the

349   uncertainty of the thermometers), showing the cross-check validity of the $Fe^{3+}/\Sigma Fe$

350   estimation. A variation of the $Fe^{3+}/\Sigma Fe$ ratio from 0 to ~23% in chlorites implies a decrease in

351   the temperatures calculated by the Inoue model of 20, 40, and 46°C depending on the sample.

352   Figure 9 displays an example of $Fe^{3+}/\Sigma Fe$ mapping at the nanometer-scale derived

353   from images at 706, 708.7, 710.25, and 718 eV using Eq. (2) (see Figure 4). The analysis was

354   carried out on the Glarus GL07 20 FIB foil. The scanned area measures 3.3 x 3.5 micrometers

355   with a pixel size of 88 nm x 88 nm. The analysis of the illite-chlorite contacts by AEM

356   showed that they are approximately perpendicular to the FIB foil surface, i.e., there is only a

357   little overlap between the two minerals at their contact. The spatial averaging effect of the x-

358   ray beam over the pixel size (i.e., 88 nm) sets the limit of the minimum distance over which

359   illite-chlorite contacts can be discriminated. Beyond this distance, the intracrystalline

360   variation of the $Fe^{3+}/\Sigma Fe$ ratio in the illite-like phase can be interpreted as an authentic

361   zonation, from ~55% in crystal rims (conforming to the spectra presented in Figure 8) to

362   ~85% in several crystal core clusters. In the same way, the $Fe^{3+}/\Sigma Fe$ ratio distribution draws a

363   subtle zonation in the chlorite, with a $Fe^{3+}/\Sigma Fe$ ratio ranging from 18 to ~23% on the crystal

364   rim, in accordance with the spectra shown in Figure 8. Such variations of the $Fe^{3+}/\Sigma Fe$ ratio

365   within the crystals are equivalent to several degrees or tens of degrees in the temperature

366   estimation, especially when this variation is associated with a variation in composition. One

367   can expect that this zonation is a crucial issue in application of geothermometers (de Andrade

368   et al. 2006; Bourdelle et al. 2013a), and the redox gap between illite and chlorite raises the

369   issue of the crystallisation processes.

11

370   In summary, the STXM-based XANES study of FIB foils from the Glarus,

371   Switzerland samples enables (i) estimation of the $Fe^{3+}/\Sigma Fe$ ratio in each phase preserving the

372   mineral texture, and (ii) establishment of iron redox mapping with high spatial resolution.

373

374   **Conclusion**

375

376   In this study, we have demonstrated the reliability of two methods that allow

377   quantitative determination of $Fe^{3+}/\Sigma Fe$ ratios in silicate phases using STXM coupled with

378   XANES spectroscopy at the Fe $L_{2,3}$-edges. These approaches are similar to those proposed by

379   van Aken and Liebscher (2002) for EELS measurements but are here calibrated for STXM.

380   The two calibrations are based on reference samples with variable but known $Fe^{3+}/\Sigma Fe$ ratios,

381   which were prepared as powders or as FIB foils. We tested these calibrations on three FIB

382   foils extracted from field samples of phyllosilicates (Glarus, Switzerland chlorite and illite

383   samples from metapelites), demonstrating the potential of these methods for quantifying

384    $Fe^{3+}/\Sigma Fe$ ratios at the submicrometer-scale. This approach will allow more quantitative

385   mineralogical or geomicrobiological studies requiring estimation of the iron redox state at the

386   nanoscale for terrestrial or extraterrestrial Fe-rich samples.

387

398

399   **References**

400

401   Bajt S, Sutton SR, Delaney JS (1994) X-ray microprobe analysis of iron oxidation-states in

402   silicates and oxides using X-ray-absorption near-edge structure (XANES). Geochim

403   Cosmochim Ac 58 (23):5209-5214

404   Beaufort D, Patrier P, Meunier A, Ottaviani MM (1992) Chemical variations in assemblages

405   including epidote and/or chlorite in the fossil hydrothermal system of Saint Martin (Lesser

406   Antilles). J Volcanol Geoth Res 51:95-114

407   Benzerara K, Miot J, Morin G, Ona-Nguema G, Skouri-Panet F, Ferard C (2011)

408   Significance, mechanisms and environmental implications of microbial biomineralization. C

409   R Geosci 343 (2-3):160-167

410   Benzerara K, Menguy N, Obst M, Stolarski J, Mazur M, Tylisczak T, Brown, Jr., GE,

411   Meibom A (2011) Study of the Crystallographic Architecture of Corals at the Nanoscale by

412   Scanning Transmission X-ray Microscopy and Transmission Electron Microscopy.

413   Ultramicroscopy 111 (8): 1268‑1275 Bernard S, Benzerara K, Beyssac O, Brown, Jr., GE

414   (2010) Multiscale characterization of pyritized plant tissues in blueschist facies

415   metamorphic rocks. Geochim Cosmochim Ac 74 (17):5054-5068

416   Berry AJ, O'Neill HS, Jayasuriya KD, Campbell SJ, Foran GJ (2003) XANES calibrations for

417   the oxidation state of iron in a silicate glass 88 (7):967-977

418   Berry AJ, Yaxley GM, Woodland AB, Foran GJ (2010) A XANES calibration for

419   determining the oxidation state of iron in mantle garnet. Chem Geol 278 (1-2):31-37

420   Bluhm, H., Andersson, K., Araki, T., Benzerara, K., Brown, J.G.E., Dynes, J.J., Ghosal, S.,

421   Gilles, M.K., Hansen, H.C., Hemminger, J.C., Hitchcock, A.P., Ketteler, G., Kilcoyne,

422   A.L.D., Kneedler, E., Lawrence, J.R., Leppard, G.G., Majzlam, J., Mun, B.S., Myneni,

423   S.C.B., Nilsson, A., Ogasawara, H., Ogletree, D.F., Pecher, K., Salmeron, M., Shuh, D.K.,

424   Tonner, B., Tyliszczak, T., Warwick, T. Yoon, T.H., 2006. Soft Xray microscopy and

425   spectroscopy at the molecular environmental science beamline at the advanced light source.

426   J Electron Spectrosc 150:86-104

427   Bolfan-Casanova N, Munoz M, McCammon C, Deloule E, Ferot A, Demouchy S, France L,

428   Andrault D, Pascarelli S (2012) Ferric iron and water incorporation in wadsleyite under

429   hydrous and oxidizing conditions: A XANES, Mossbauer, and SIMS study. Am Mineral 97

430   (8-9):1483-1493

431   Boulard E, Menguy N, Auzende AL, Benzerara K, Bureau H, Antonangeli D, Corgne A,

432   Morard G, Siebert J, Perrillat JP, Guyot F, Fiquet G (2012) Experimental investigation of

433   the stability of Fe-rich carbonates in the lower mantle. J Geophys Res-Solid Earth 117

434   Bourdelle F, Parra T, Beyssac O, Chopin C, Moreau F (2012) Ultrathin section preparation of

435   phyllosilicates by Focused Ion Beam milling for quantitative analysis by TEM-EDX. Appl

436   Clay Sci 59-60:121-130

437 Bourdelle F, Parra T, Beyssac O, Chopin C, Vidal O (2013a) Clay minerals as geo-
438   thermometer: A comparative study based on high-spatial-resolution analyses of illite and
439   chlorite in Gulf Coast sandstones (Texas, USA). Am Mineral 98 (5-6):914-926

440 Bourdelle F, Parra T, Chopin C, Beyssac O (2013b) A new chlorite geothermometer for
441   diagenetic to low-grade metamorphic conditions. Contrib Mineral Petr 165:723-735

442 Brotton SJ, Shapiro R, van der Laan G, Guo J, Glans PA, Ajello JM (2007) Valence state
443   fossils in Proterozoic stromatolites by L-edge X-ray absorption spectroscopy. J Geophys
444   Res-Biogeosci 112 (G3)

445 Carlut J, Benzerara K, Horen H, Menguy N, Janots D, Findling N, Addad A, Machouk I
446   (2010) Microscopy study of biologically mediated alteration of natural mid-oceanic ridge
447   basalts and magnetic implications. J Geophys Res-Biogeosci 115

448 Chen CT, Idzerda YU, Lin HJ, Smith NV, Meigs G, Chaban E, Ho GH, Pellegrin E, Sette F
449   (1995) Experimental Confirmation of the X-Ray Magnetic Circular-Dichroism Sum-Rules
450   for Iron and Cobalt. Phys Rev Lett 75 (1):152-155

451 Cressey G, Henderson CMB, Vanderlaan G (1993) Use of L-edge X-Ray-Absorption
452   Spectroscopy to Characterize Multiple Valence States of 3d Transition-Metals - a New
453   Probe for Mineralogical and Geochemical Research. Phys Chem Miner 20 (2):111-119

454 Crocombette JP, Pollak M, Jollet F, Thromat N, Gautiersoyer M (1995) X-Ray-Absorption
455   Spectroscopy at the Fe L(2,3) Threshold in Iron-Oxides. Phys Rev B 52 (5):3143-3150

456 de Andrade V, Vidal O, Lewin E, O'Brien P, Agard P (2006) Quantification of electron
457   microprobe compositional maps of rock thin sections: an optimized method and examples. J
458   Metamorph Geol 24 (7):655-668

459 de Groot FMF, de Smit E, van Schooneveld MM, Aramburo LR, Weckhuysen BM (2010) In-
460   situ Scanning Transmission X-Ray Microscopy of Catalytic Solids and Related
461   Nanomaterials. ChemPhysChem 11 (5):951-962

462 de Smit E, Swart I, Creemer JF, Hoveling GH, Gilles MK, Tyliszczak T, Kooyman PJ,
463   Zandbergen HW, Morin C, Weckhuysen BM, de Groot FMF (2008) Nanoscale chemical
464   imaging of a working catalyst by scanning transmission X-ray microscopy. Nature 456
465   (7219):222-U239

466 Fialin M, Bézos A, Wagner C, Magnien V, Humler E (2004) Quantitative electron
467   microprobe analysis of $Fe^{3+}/\Sigma Fe$: Basic concepts and experimental protocol for glasses. Am
468   Mineral 89 (4):654-662

469 Garvie LA, Zega TJ, Rez P, Buseck PR (2004) Nanometer-scale measurements of $Fe^{3+}/\Sigma Fe$
470   by electron energy-loss spectroscopy: A cautionary note. Am Mineral 89 (11-12):1610-1616

471   Hanhan S, Smith AM, Obst M, Hitchcock AP (2009) Optimization of analysis of soft X-ray

472   spectromicroscopy at the Ca 2p edge. J Electron Spectrosc 173 (1):44-49

473   Heaney PJ, Vicenzi EP, Giannuzzi LA, Livi KJT (2001) Focused ion beam milling: A method

474   of site-specific sample extraction for microanalysis of Earth and planetary materials. Am

475   Mineral 86 (9):1094-1099

476   Heijboer WM, Battiston AA, Knop-Gericke A, Havecker M, Mayer R, Bluhm H, Schlogl R,

477   Weckhuysen BM, Koningsberger DC, de Groot FMF (2003) In-situ soft X-ray absorption of

478   over-exchanged Fe/ZSM5. J Phys Chem B 107 (47):13069-13075

479   Hitchcock AP (2012) aXis 2000 Analysis of X-ray Images and Spectra. McMaster University,

480   Hamilton, ON, Canada

481   Inoue A, Meunier A, Patrier-Mas P, Rigault C, Beaufort D, Vieillard P (2009) Application of

482   chemical geothermometry to lowtemperature trioctahedral chlorites. Clay Clay Miner

483   57(3):371–382

484   Joswig W, Amthauer G, Takeuchi Y (1986) Neutron-diffraction and Mössbauer spectroscopic

485   study of clintonite (xanthophyllite). Am Mineral 71:1194-1197

486   Keeling JL, Raven MD, Gates WP (2000) Geology and characterization of two hydrothermal

487   nontronites from weathered metamorphic rocks at the Uley Graphite Mine, South Australia.

488   Clay Clay Miner 48 (5):537-548

489   Lahfid A, Beyssac O, Deville E, Negro F, Chopin C, Goffe B (2010) Evolution of the Raman

490   spectrum of carbonaceous material in low-grade metasediments of the Glarus Alps

491   (Switzerland). Terra Nova 22 (5):354-360

492   Lam KP, Hitchcock AP, Obst M, Lawrence JR, Swerhone GDW, Leppard GG, Tyliszczak T,

493   Karunakaran C, Wang J, Kaznatcheev K, Bazylinski DA, Lins U (2010) Characterizing

494   magnetism of individual magnetosomes by X-ray magnetic circular dichroism in a scanning

495   transmission X-ray microscope. Chem Geol 270 (1-4):110-116

496   Lauterbach S, McCammon CA, van Aken P, Langenhorst F, Seifert F (2000) Mossbauer and

497   ELNES spectroscopy of $(Mg,Fe)(Si,Al)O_3$ perovskite: a highly oxidised component of the

498   lower mantle. Contrib Mineral Petr 138 (1):17-26

499   Magnien V, Neuville DR, Cormier L, Mysen BO, Briois V, Belin S, Pinet O, Richet P (2004)

500   Kinetics of iron oxidation in silicate melts: a preliminary XANES study. Chem Geol 213 (1-

501   3):253-263

502   Miot J, Benzerara K, Morin G, Kappler A, Bernard S, Obst M, Ferard C, Skouri-Panet F,

503   Guigner JM, Posth N, Galvez M, Brown, Jr., GE, Guyot F (2009) Iron biomineralization by

504   anaerobic neutrophilic iron-oxidizing bacteria. Geochim Cosmochim Ac 73 (3):696-711

505 Miot J, Maclellan K, Benzerara K, Boisset N (2011) Preservation of protein globules and
506 peptidoglycan in the mineralized cell wall of nitrate-reducing, iron(II)-oxidizing bacteria: a
507 cryo-electron microscopy study. Geobiology 9 (6):459-470

508 Munoz M, De Andrade V, Vidal O, Lewin E, Pascarelli S, Susini J (2006) Redox and
509 speciation micromapping using dispersive X-ray absorption spectroscopy: Application to
510 iron chlorite mineral of a metamorphic rock thin section. Geochem Geophys Geosyst 7

511 Raabe, J., Tzvetkov, G., Flechsig, U., Böge, M., Jaggi, A., Sarafimov, B., Vernooij, M.G.C.,
512 Huthwelker, T., Ade, H., Kilcoyne, D., Tyliszczak, T., Fink, R.H. Quitmann, C., 2008.
513 PolLux: A new facility for soft X-ray spectromicroscopy at the Swiss Light Source. Rev Sci
514 Instrum 79

515 Raeburn SP, Ilton ES, Veblen DR (1997a) Quantitative determination of the oxidation state of
516 iron in biotite using X-ray photoelectron spectroscopy: I. Calibration. Geochim Cosmochim
517 Ac 61 (21):4519-4530

518 Raeburn SP, Ilton ES, Veblen DR (1997b) Quantitative determination of the oxidation state of
519 iron in biotite using X-ray photoelectron spectroscopy: II. In situ analyses. Geochim
520 Cosmochim Ac 61 (21):4531-4537

521 Rigault C (2010) Cristallochimie de Fer dans les chlorites de basse température : implications
522 pour la géothermométrie et la détermination des paléoconditions redox dans les gisements
523 d'Uranium. University of Poitiers, Poitiers

524 Schingaro E, Scordari F, Mesto E, Brigatti MF, Pedrazzi G (2005) Cation-site partitioning in
525 Ti-rich micas from Black Hill (Australia): A multi-technical approach. Clay Clay Miner 53
526 (2):179-189

527 Schmid R, Wilke M, Oberhänsli R, Janssens K, Falkenberg G, Franz L, Gaab A (2003)
528 Micro-XANES determination of ferric iron and its application in thermobarometry. Lithos
529 70 (3-4):381-392

530 Stagno V, Ojwang DO, McCammon CA, Frost DJ (2013) The oxidation state of the mantle
531 and the extraction of carbon from Earth's interior. Nature 493: 84-88

532 van Aken PA, Liebscher B (2002) Quantification of ferrous/ferric ratios in minerals: new
533 evaluation schemes of Fe L-23 electron energy-loss near-edge spectra. Phys Chem Miner 29
534 (3):188-200

535 van der Laan G, Kirkman IW (1992) The 2p Absorption-Spectra of 3d Transition-Metal
536 Compounds in Tetrahedral and Octahedral Symmetry. J Phys-Condes Matter 4 (16):4189-
537 4204

538 Wasinger EC, de Groot FMF, Hedman B, Hodgson KO, Solomon EI (2003) L-edge X-ray

539   absorption spectroscopy of non-heme iron sites: Experimental determination of differential

540   orbital covalency. J Am Chem Soc 125 (42):12894-12906

541 Waychunas GA, Apted MJ, Brown, Jr., GE (1983) X-ray K-edge absorption spectra of Fe

542   minerals and model compounds: Near-edge structure. Phy Chem Min 10 (1):1-9

543 Wilke M, Farges F, Petit PE, Brown, Jr., GE, Martin F (2001) Oxidation state and

544   coordination of Fe in minerals: An FeK-XANES spectroscopic study. Am Mineral 86 (5-

545   6):714-730

546 Wilke M, Hahn O, Woodland AB, Rickers K (2009) The oxidation state of iron determined

547   by Fe K-edge XANES-application to iron gall ink in historical manuscripts. J Anal Atom

548   Spectrom 24 (10):1364-1372

549

550 **Tables**

551

552 **Table 1** Reference samples used for XANES - $Fe^{3+}/\Sigma Fe$ ratio quantification

553

Type	Sample	Source	FeO %wt.*	$Fe^{3+}/\Sigma Fe$ Redox ratio	Position of maximum peak intensity (eV)			
					L_3-a	L_3-b	L_2-a	L_2-b
Silicate glass	PyrNa	Magnien et al. (2004)	12.83	0.73 ±0.03	708.57	710.04	721.68	723.54
Silicate glass	PyrNa17R	Magnien et al. (2004)	12.75	0.09 ±0.01	708.36	710.77	721.37	723.54
Silicate glass	PyrNa5R	Magnien et al. (2004)	12.92	0.61 ±0.01	708.57	710.04	721.68	723.54
Silicate glass	PyrNa750	Magnien et al. (2004)	12.68	0.94 ±0.03	708.67	710.25	721.68	723.54
Silicate glass	PyrNa1200	Magnien et al. (2004)	13.52	0.89 ±0.05	708.67	708.93	721.84	724.54
Nesosilicate	Fayalite	Neuville D.	70.50	0.00 ±0.00‡	708.09	710.71	720.75	723.54
Phyllosilicate	Smectite Nau-2	Keeling et al. (2000)	34.10	1.00 ±0.00‡	708.57	710.35	721.84	723.54
Phyllosilicate	Clintonite	Joswig et al. (1986)	3.01	0.69 ±0.03‡	708.25	710.08	721.49	723.53
Phyllosilicate	Ti-mica	Shingaro et al. (2005)	19.38	0.03 ±0.03‡	708.04	710.04	721.00	723.54
Phyllosilicate	Chlorite 'Prochlorite'	MNHN†	14.50	0.30 ±0.10‡	708.26	710.21	721.51	723.51
Phyllosilicate	Chlorite Ch1	This study	40.10	0.17 ±0.05	708.04	710.19	721.00	723.54
Phyllosilicate	Chlorite GAB 42	Rigault (2010)	28.50	0.14 ±0.03	708.15	710.46	720.75	723.54
Phyllosilicate	Chlorite VNI 92	Rigault (2010)	20.73	0.35 ±0.03	708.15	710.25	720.75	723.54
Phyllosilicate	Chlorite VNI 114	Rigault (2010)	20.82	0.20 ±0.03	708.04	710.25	720.75	723.54

554 * ΣOxides wt% = 100 as basis and all iron reported as ferrous. † MNHN: Collection of Muséum National

555 d'Histoire Naturelle, France. ‡ assumed error deviation.

556

17

557 **Table 2** AEM chemical representative analyses of Glarus chlorites and comparison of

558 thermometers results taking into account $Fe^{3+}/\Sigma Fe$ ratios (Eq. (3)); regarding the scatter of

559 data on Figure 3, we infer a precision of ±5% on the $Fe^{3+}/\Sigma Fe$. Analyses were carried out on

560 crystal rims, along the illite-chlorite contact, according to Bourdelle et al. (2013a).

561 Temperature estimations were performed with Bourdelle et al. (2013b) and Inoue et al. (2009)

562 thermometers, with and without consideration of Fe^{3+}, in accordance with the

563 recommendations made by each authors. Taking into account the $Fe^{3+}/\Sigma Fe$ ratios in the Inoue

564 model allows to obtain similar results to those calculated with the Bourdelle model (which is

565 a pure Fe^{2+} model), i.e., with a difference less than 30°C (equivalent to the uncertainty of each

566 model)

567

Chlorite [%wt]	GL07 13	GL07 20	GL07 16
SiO_2	32.70	31.40	31.57
TiO_2	0.07	0.06	0.04
Al_2O_3	26.41	25.56	26.02
FeO	26.63	28.53	25.13
MnO	0.00	0.00	0.00
MgO	13.75	13.97	16.70
CaO	0.06	0.10	0.29
Na_2O	0.00	0.04	0.00
K_2O	0.39	0.35	0.25
$Fe^{3+}/\Sigma Fe$ [%]	22.30	23.80	27.90
T_{BOU} [°C]	135	170	182
$T_{INO-Fe2+}$ [°C]	165 (*+30*)	236 (*+66*)	258 (*+76*)
$T_{INO-Fe3+}$ [°C]	145 (*+10*)	196 (*+26*)	210 (*+28*)

568 T_{BOU}: temperatures calculated with the Fe^{2+}-pure model of Bourdelle et al. (2013b), considering $Fe_{tot} = Fe^{2+}$.

569 $T_{INO-Fe2+}$: temperatures calculated with the Inoue et al. (2009) model, considering $Fe_{tot} = Fe^{2+}$. $T_{INO-Fe3+}$:

570 temperatures calculated with the Inoue et al. (2009) model, using the estimated $Fe^{3+}/\Sigma Fe$.
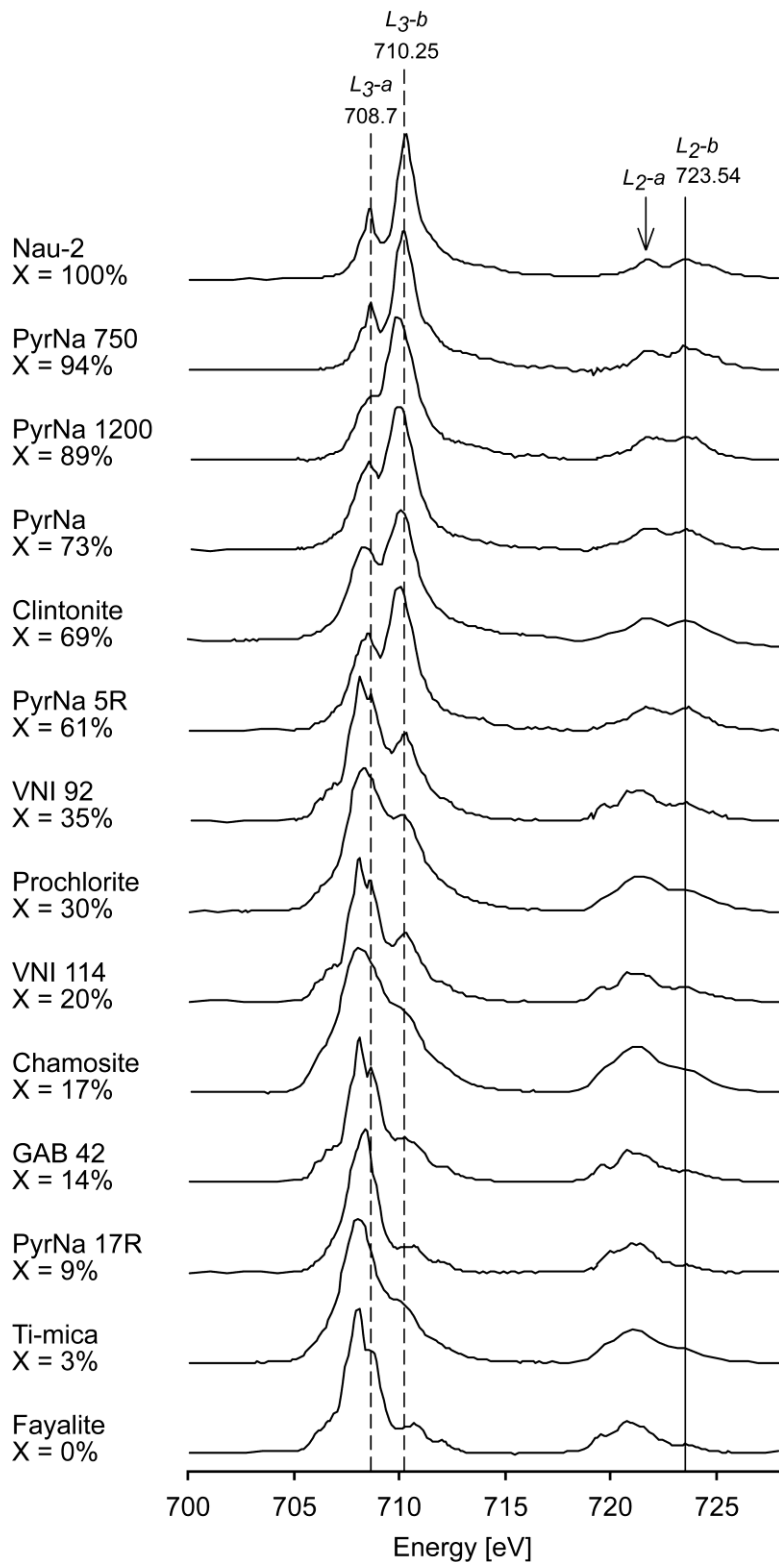
571

572 **Figures**

573

574
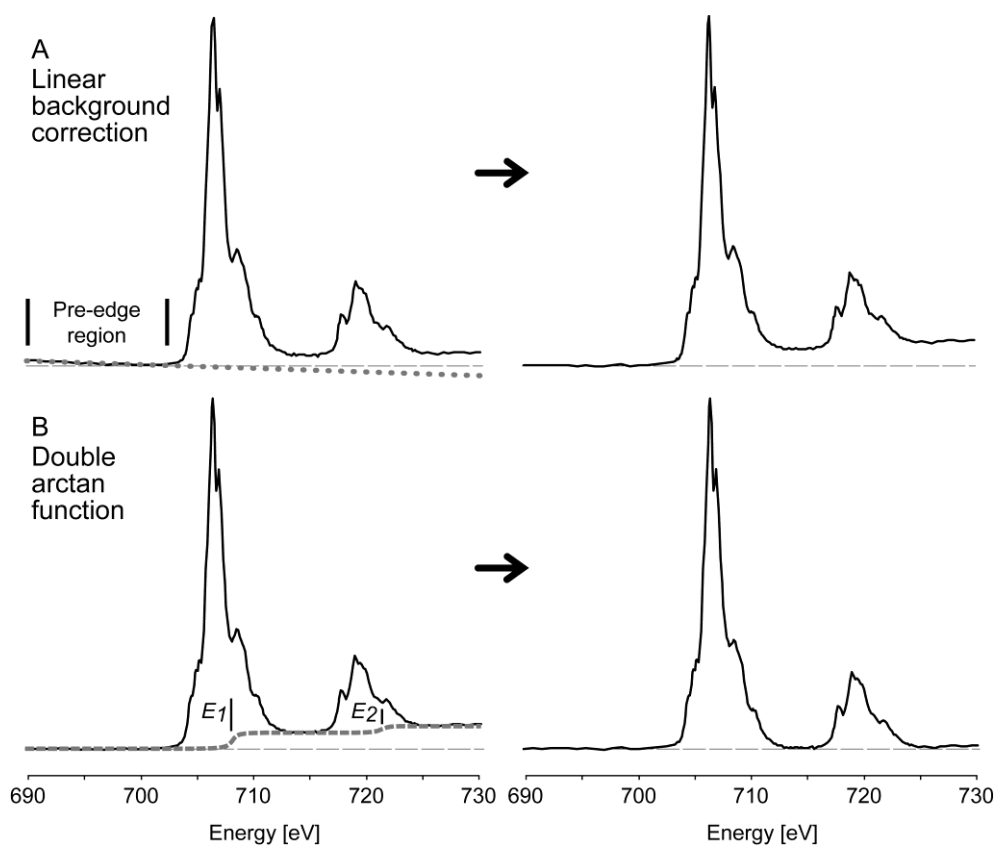
Fig. 1 Subtraction of background from XANES spectra at Fe L-edge, using linear and double

arctan functions ($w_1 = w_2 = 1$ eV), for chlorite GAB 42

577

578

Fig. 2 Representative XANES spectra at the Fe L₂,₃-edges for the reference silicates. The

spectra have been normalised to the integral Fe L₃-edge intensity, and some of the spectra

have been shifted vertically for clarity (normalized intensity with arbitrary units). The dotted

lines represent the energies fixed to determine the Fe^{3+} concentration from the Fe L₃-peaks'

583   intensity ratio. The solid line underlines the position of L_2-b maximum intensity, which is

584   identical for all spectra. X = $Fe^{3+}/\Sigma Fe$ ratios of Table 1

585
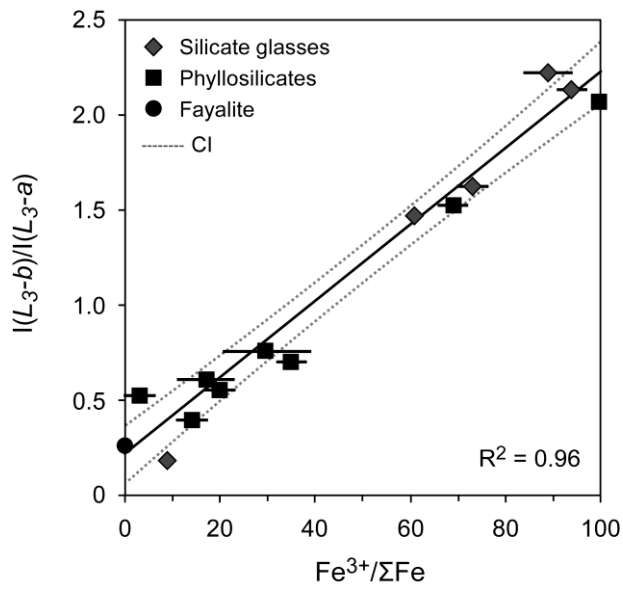
586

587   **Fig. 3** L_3-edge intensity ratio *I(L_3-b)/I(L_3-a)* from XANES spectra versus ferric iron

588   concentration $Fe^{3+}/\Sigma Fe$ quantified by independent methods for the selected silicates. CI:

589   confidence interval (95%)

590

21
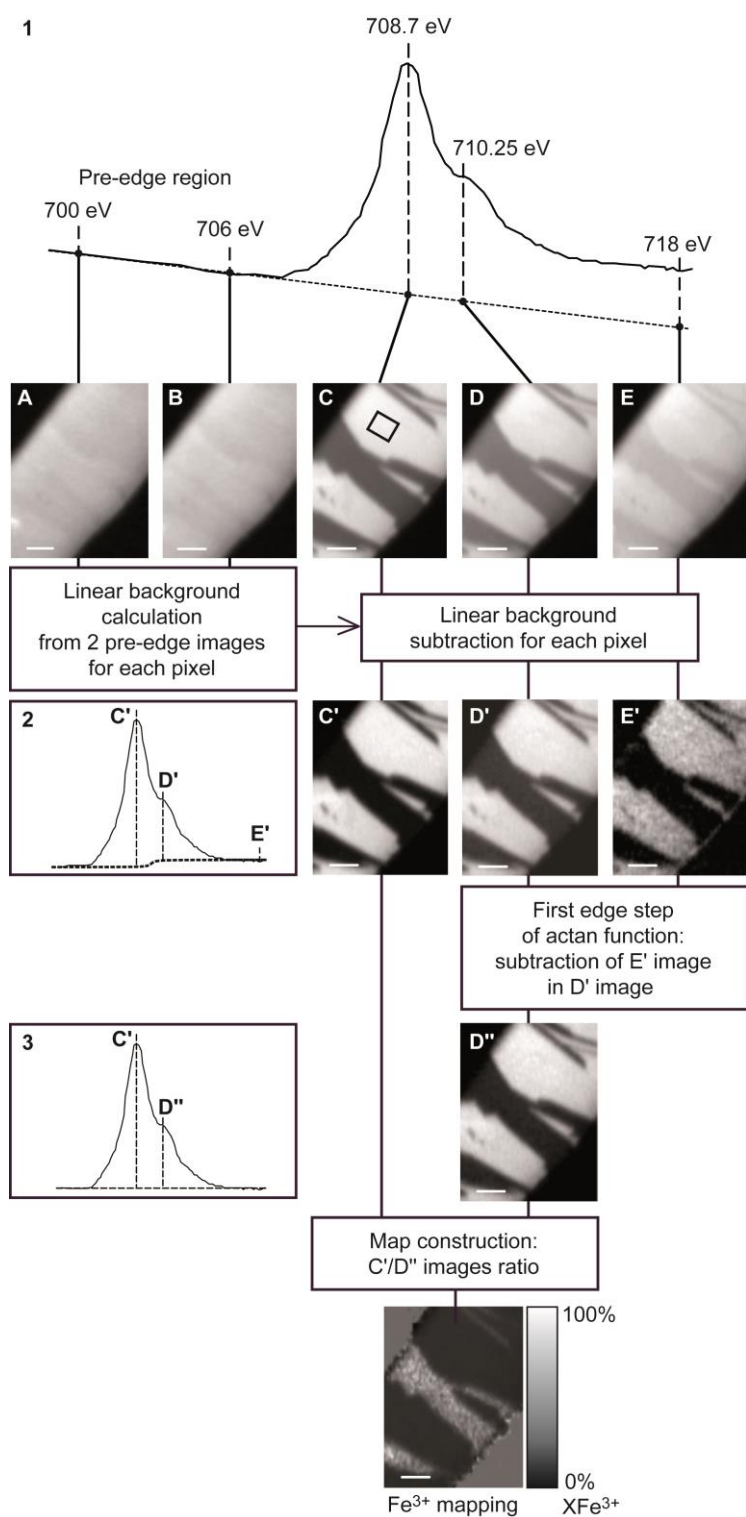
Fig. 4 Determination of the $Fe^{3+}/\Sigma Fe$ ratio from 5 selected energy images: two images in the pre-edge (to apply the "linear background correction" at each pixel of the image), one at 708.7 eV to quantify the L_3-a peak, one at 710.25 eV to quantify the L_3-b peak, and one at 718 eV, to remove the edge step of the arctan function. Finally, the ratio of the resulting 708.7 and 710.25 eV images can be used to determine the R_{L3} parameter at each pixel of the image, and obtain iron redox mapping. All images are OD images (70 x 90 pixels), where the illite and

598   chlorite are the dark- and light- grey phases, respectively. As an illustration, spectrum #1 was

599   retrieved from 110 images (i.e., 110 energy points) on a chlorite area (dark rectangle on image

600   C); spectrum #2 was obtained after the linear function subtraction from spectrum #1 and

601   spectrum #3 after the actan function subtraction from spectrum #2. Case of FIB foil of Glarus

602   GL07 20 sample.

603
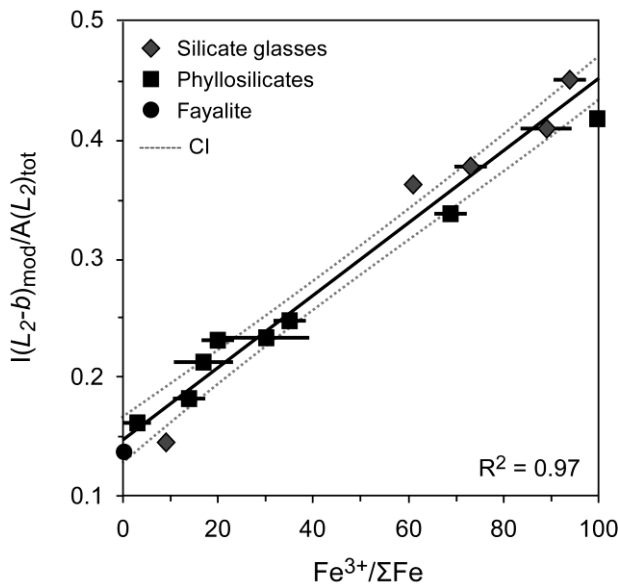
604

605   **Fig. 5** L_2-edge integral intensity ratio (i.e., integral intensity of maximum L_2-b ± 0.1 eV over

606   total integral intensity (area) of L_2-edge) from XANES spectra versus ferric iron

607   concentration $Fe^{3+}/\Sigma Fe$ quantified by independent methods for the reference silicates. CI:

608   confidence interval (95%)

609

23
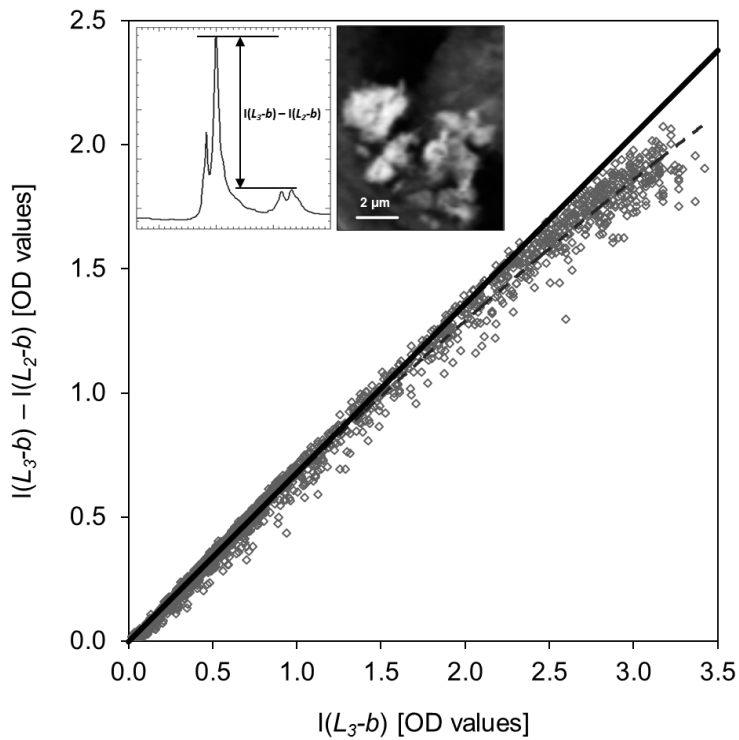
Fig. 6 Difference, pixel by pixel, of intensity detected between the 710.25 and the 723.54 eV images (in which a pre-edge image was not subtracted) versus the intensity of the 710.25 eV image of a Smectite Nau-2 STXM-map (Nau-2, 72 x 88 pixels = 6336 points), i.e., the L_3-b − L_2-b intensity difference versus the L_3-b intensity for each pixel. The dashed line was calculated from a quadratic equation. Insets: representative spectra and optical density image (710.25 eV) for Nau-2 sample

618
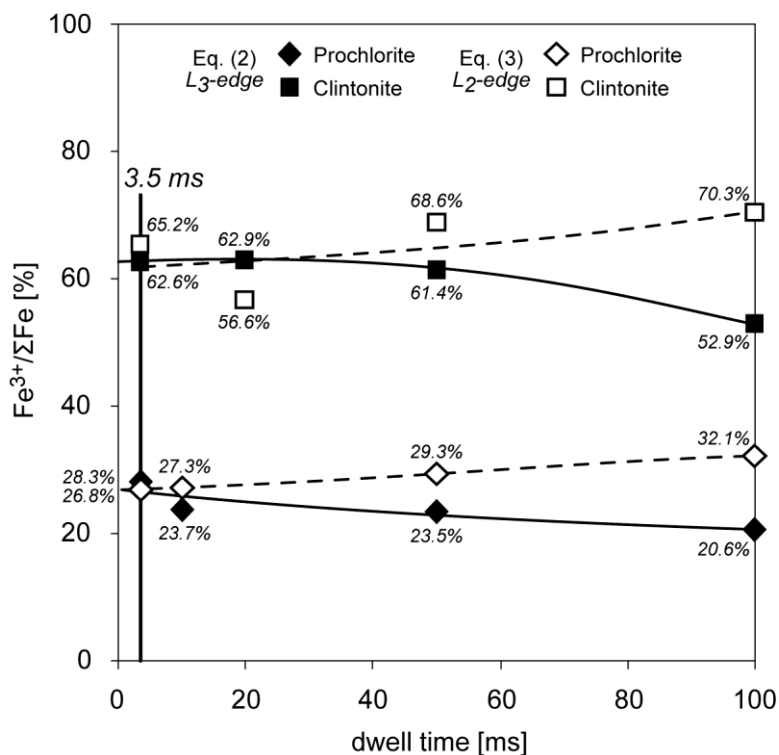
Fig. 7 Beam-induced radiation damage during STXM analyses of chlorite 'prochlorite'
(XFe^{3+} = 30%) and clintonite (XFe^{3+} = 69%). Evolution of the Fe^{3+}/ΣFe ratios as a function of
dwell time, estimated by Eq. (2) and (3) from XANES spectra. Data were fit by a quadratic
function. The beam radiations (increasing dwell) involve (1) a decrease of XFe^{3+} calculated
from L$_3$-edge (Eq. 2) and (2) an increase of XFe^{3+} calculated from L$_2$-edge (Eq. 3). Spectra of
reference samples and Glarus samples (see text) were recorded with a dwell time of 1.3-
3.5 ms per point and energy: the beam radiation damage is thus negligible with our analytical
conditions for data collection
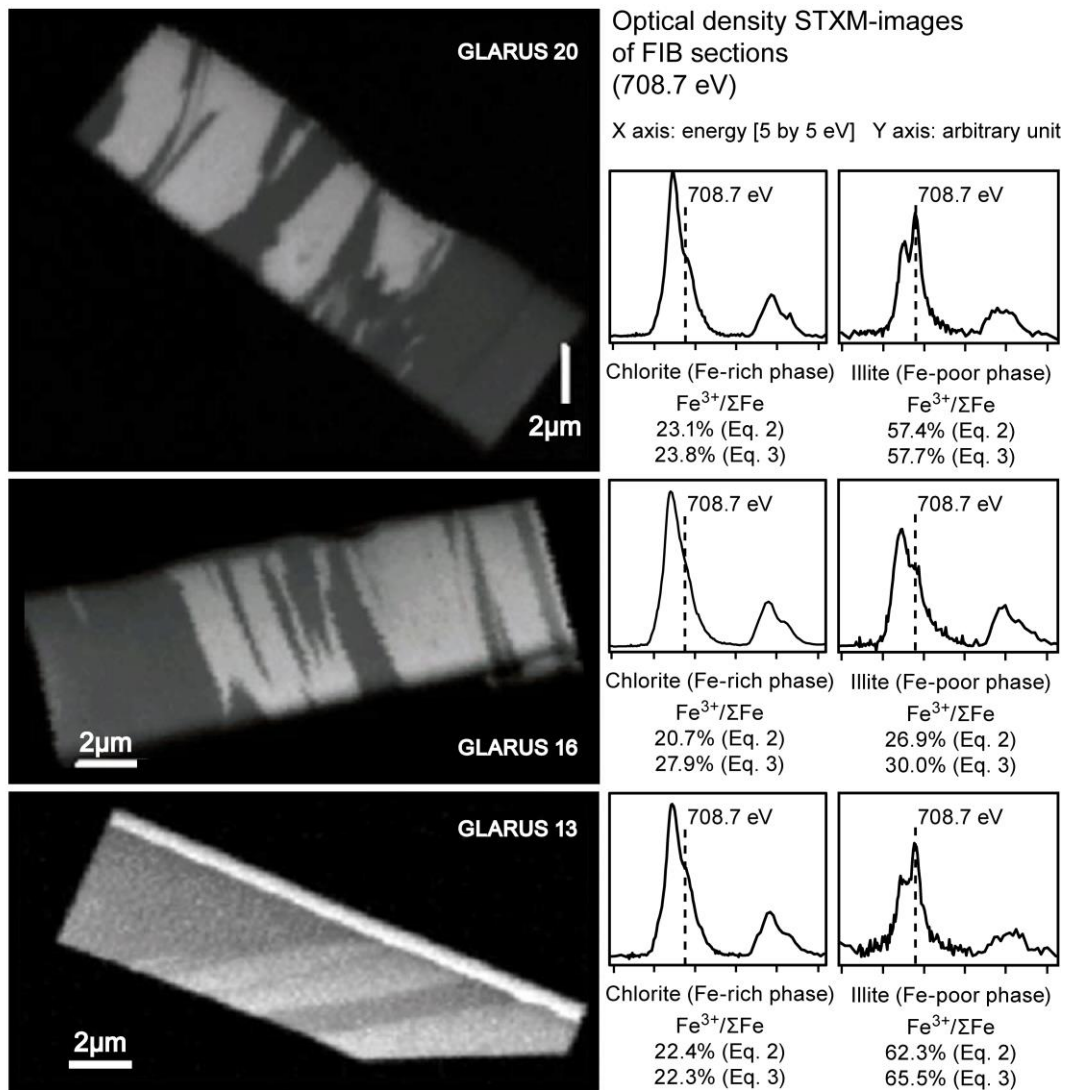
Fig. 8 Scanning transmission x-ray microscopy (STXM) and XANES analysis and $Fe^{3+}/\Sigma Fe$ estimations for FIB foils of Glarus samples (chlorite and illite). [Left] Optical density images of FIB foils at 708.7 eV. The illite and chlorite are the dark- and light- grey phases, respectively. [Right] XANES spectra of areas of interest and calculated Fe^{3+} concentrations associated (crystals rims)
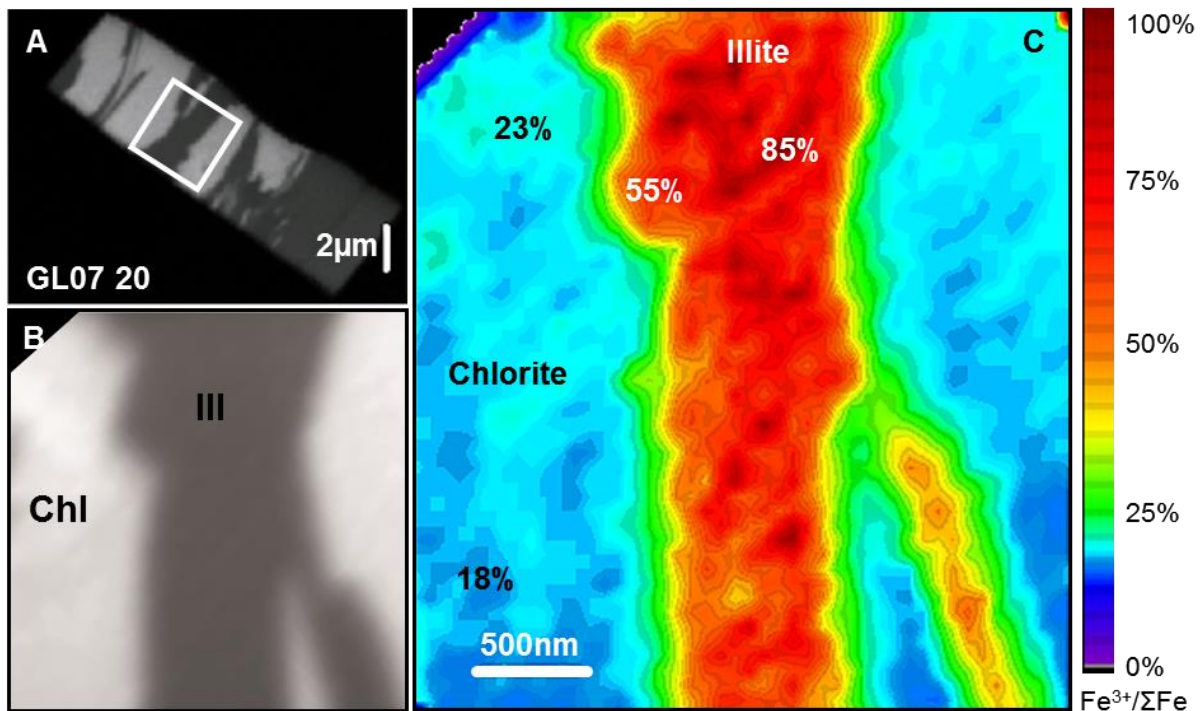
Fig. 9 Quantitative Fe redox nanomapping on FIB foil of Glarus GL07 20 sample. (a) Optical density image at 708.7 eV of Glarus GL07 20 FIB section, where the illite and chlorite are the dark- and light- grey phases, respectively. (b) Optical density image at 708.7 eV of the area of interest. (c) iron redox mapping, calculated from the 708.7 to 710.25 eV images ratio coupled with Eq. (2). The illite-chlorite contacts were analysed by AEM to check that they are approximately perpendicular to the FIB foil surface, i.e., there is only a small overlap between the two minerals at their contact. The spatial averaging effect of the x-ray beam over the pixel size (i.e., 88 nm) sets the limit of the minimum distance over which illite-chlorite contacts can be discriminated. Beyond this distance, the intracrystalline variation of $Fe^{3+}/\Sigma Fe$ ratio in the illite-like phase can be interpreted as an authentic zonation, from 55% to 85% in several crystal core clusters